Directional Graph Flow and Koopman-Inspired Dynamics for Probabilistic Land Deformation Prediction

Jiansong Yang*, Tao Li*, Hanbo Yang*, Yan Liu†, and Xovee Xu†
*CHN Energy Dehong Power Generation Co., Ltd., Dehong, Yunnan, China
†University of Electronic Science and Technology of China, Chengdu, Sichuan, China
Emails: {12109784, 12055266, 20090205}@ceic.com, yan.liu@std.uestc.edu.cn, xovee@uestc.edu.cn (Corresponding)

***Abstract*—Accurate forecasting of land deformation is important for safety monitoring in landslide-prone slopes, reservoirs, dams, and other critical infrastructure. This problem remains difficult because deformation fields exhibit strong spatiotemporal dependence, terrain-induced anisotropy, and non-stationary temporal dynamics. We propose DKLand, a probabilistic forecasting framework that retains a deformation-aware dynamic graph backbone while improving both spatial and temporal modeling. For spatial modeling, DKLand introduces a directional graph flow encoder that learns continuous edge directions and performs asymmetric message passing, producing more informative terrain-aware representations. For temporal modeling, DKLand uses a Koopman-inspired non-autonomous neural ODE forecaster whose parameters vary over time, which improves adaptation to non-stationary behavior and regime changes. Experiments on two real-world InSAR datasets, HZY and PBG, show that DKLand consistently outperforms strong baselines.**

***Index Terms*—land deformation prediction, graph neural network, neural ODEs, probabilistic forecasting**

I. Introduction

Land deformation, including subsidence and uplift, may develop gradually or occur abruptly. Its effects can be severe around hydropower stations, reservoir dams, and unstable slopes, where progressive displacement may threaten operational safety and even lead to catastrophic failures [1], [2]. Land deformation also affects urban buildings, transportation networks, and other critical facilities [3]. Accurate forecasting of future deformation is therefore valuable for risk assessment, early warning, and infrastructure management.

Satellite-based Interferometric Synthetic Aperture Radar (InSAR) has become a major tool for this problem because it can measure subtle ground motion over large and hard-to-access areas. Compared with traditional point-based surveying, InSAR provides much denser spatial coverage and supports continuous monitoring of complex terrains such as steep reservoir banks and long infrastructure corridors [4]. These advances have greatly increased the availability of deformation time series for predictive modeling. Reliable forecasting, however, remains difficult. Deformation fields often show strong spatiotemporal dependence, clear terrain-induced anisotropy, and non-stationary temporal patterns driven by hydrology, reservoir operations, and human activity. Local deformation behavior may also differ substantially across geological and topographic conditions. These properties call for forecasting models that capture fine-grained spatial interactions and remain accurate over long prediction horizons.

Over the past two decades, research on land deformation and landslide hazards has moved from measurement-focused monitoring to data-driven prediction. Early studies relied on multi-temporal InSAR time-series methods, such as Persistent Scatterer InSAR and Small Baseline Subset, to recover reliable wide-area deformation trajectories from satellite observations [5], [6]. Based on these deformation products and environmental conditioning factors, early hazard assessment often used statistical and classical machine learning methods, such as logistic regression and random forests, for factor-based landslide susceptibility analysis [7], [8]. These methods are interpretable and effective with informative hand-crafted factors, but are limited in modeling complex nonlinear and spatiotemporal dependencies [9]. As larger multi-source datasets became available, researchers adopted deep neural networks to capture nonlinear relationships more effectively, including CNN-based models for spatial patterns and recurrent models such as LSTMs for deformation sequences [10], [11]. These models learn richer data-driven representations, but many early approaches emphasize either spatial or temporal modeling rather than both jointly [12]. Recent studies model space and time more explicitly, for example [13], [14]. In land deformation forecasting, DyLand [15] marked an important step toward probabilistic spatiotemporal modeling. Even so, long-horizon prediction under non-stationary dynamics and complex terrain interactions remains difficult.

Two limitations remain. First, although DyLand learns time-varying adjacency from both terrain locations and deformation history, its spatial encoder still relies on standard neighborhood aggregation. This design does not explicitly represent directional or asymmetric influence between nearby locations, even though terrain interactions on real slopes are often anisotropic. Relative elevation, slope orientation, and local surface structure can all produce unequal influence across directions. Second, DyLand uses a neural-ODE-based continuous-time forecasting formulation, but its vector field is governed by fixed network weights during temporal evolution. In real deformation systems, the underlying dynamics may change over time because of hydrological variation, reservoir operations, and other external disturbances. A time-invariant

979-8-3195-0733-4/26/$31.00 ©2026 IEEE

parameterization may therefore limit long-horizon prediction under non-stationary conditions.

To address these challenges, we propose DKLand, a probabilistic spatiotemporal forecasting framework for land deformation prediction. DKLand builds on DyLand and preserves its deformation-aware dynamic graph construction, while strengthening both the spatial and temporal components. For spatial modeling, DKLand introduces a directional graph flow learner that estimates continuous edge directionality and performs asymmetric message propagation. This design improves the representation of anisotropic terrain interactions. For temporal modeling, DKLand introduces a Koopman-inspired non-autonomous neural ODE whose parameters evolve over time, allowing the model to better capture structured but non-stationary deformation dynamics.

Our main contributions are as follows:

- We propose DKLand, a probabilistic spatiotemporal forecasting framework for land deformation prediction that extends the DyLand backbone with stronger spatial and temporal modeling.
- We introduce a directional graph flow spatial learner that assigns each edge a continuous directionality and performs asymmetric message propagation, improving the modeling of anisotropic interactions.
- We propose a Koopman-inspired non-autonomous neural ODE with time-evolving parameters to improve long-horizon forecasting under non-stationary dynamics.
- Extensive experiments on two real-world landslide-prone InSAR datasets, HZY and PBG, show that DKLand consistently outperforms strong baselines.

II. Methodology

We first define the land deformation forecasting problem and then present DKLand. The framework has four parts: deformation-aware dynamic graph construction, directional graph-flow spatial encoding, Koopman-inspired time-varying continuous dynamics, and probabilistic prediction.

A. Problem Definition

We study land deformation prediction over an InSAR-monitored terrain surface represented as a spatial point cloud. Let $V = \{v_i\}_{i=1}^N$ denote the set of N monitored locations, where each $v_i \in \mathbb{R}^3$ is the spatial coordinate of location i. Let $t_1 < \cdots < t_T$ denote the observed timestamps, and let

$$S = \big[s_i(t_\tau)\big]_{i=1,\ldots,N;\,\tau=1,\ldots,T} \in \mathbb{R}^{N\times T} \tag{1}$$

denote the historical deformation sequence, where $s_i(t_\tau)$ is the deformation observed at location v_i at time t_τ.

Given (V, S), the goal is to forecast future deformation at timestamps $t_{T+1}, \ldots, t_{T'}$, namely

$$Y = \big[y_i(t_\tau)\big]_{i=1,\ldots,N;\,\tau=T+1,\ldots,T'} \in \mathbb{R}^{N\times(T'-T)}, \tag{2}$$

while also quantifying predictive uncertainty. Following DyLand, we adopt a continuous-time forecasting view and learn a conditional predictive distribution $p(Y \mid V, S)$ [15], [16].

B. Overview of DKLand

DKLand extends the deformation-aware dynamic graph backbone of DyLand and improves both the spatial encoder and the temporal forecasting module. The framework consists of four stages: (1) deformation-aware dynamic graph construction from terrain geometry and historical deformation; (2) directional graph-flow spatial encoding with learned continuous edge directionality; (3) Koopman-inspired time-varying latent dynamics in continuous time; and (4) probabilistic deformation prediction with heteroscedastic uncertainty estimation. Figure 1 shows the overall architecture.

C. Deformation-Aware Dynamic Graph Construction

Following DyLand, we use a deformation-aware dynamic graph to represent time-varying dependencies among InSAR locations [15]. At each observed timestamp t_τ, we compute a latent embedding $u_i^\tau \in \mathbb{R}^{d_u}$ from terrain geometry and deformation context:

$$u_i^\tau = f_{\mathrm{man}}(v_i, s_i(t_\tau)), \tag{3}$$

where $f_{\mathrm{man}}(\cdot)$ is the dynamic manifold encoder inherited from DyLand backbone.

We define the edge affinity score between two locations as

$$\pi_{ij}^\tau = \sigma\big(-\|u_i^\tau - u_j^\tau\|_2^2\big)\,, \tag{4}$$

where $\sigma(\cdot)$ is the sigmoid function. For each node, we keep the top-k neighbors with the largest affinity scores and form a sparse adjacency matrix $A^\tau \in \{0,1\}^{N\times N}$.

The directional encoder later learns asymmetric information flow on top of an undirected support. We therefore define a symmetrized support graph as

$$\bar{A}_{ij}^\tau = \mathbf{1}\big(A_{ij}^\tau + A_{ji}^\tau > 0\big)\,. \tag{5}$$

We then compute normalized edge weights

$$\tilde{a}_{ij}^\tau = \frac{\bar{A}_{ij}^\tau}{\sum_{j'} \bar{A}_{ij'}^\tau + \epsilon}, \tag{6}$$

where $\epsilon > 0$ avoids division by zero. The resulting graph sequence $\{\bar{A}^\tau\}_{\tau=1}^T$ provides the spatial support for the directional graph-flow encoder.

D. Directional Graph Flow Encoder

A key limitation of standard graph message passing is that it mainly behaves like diffusion, which may blur anisotropic spatial interactions and obscure asymmetric influence patterns. To address this issue, DKLand introduces a directional graph-flow encoder that learns a continuous directionality for each retained edge pair and separately aggregates across two directional message channels [17].

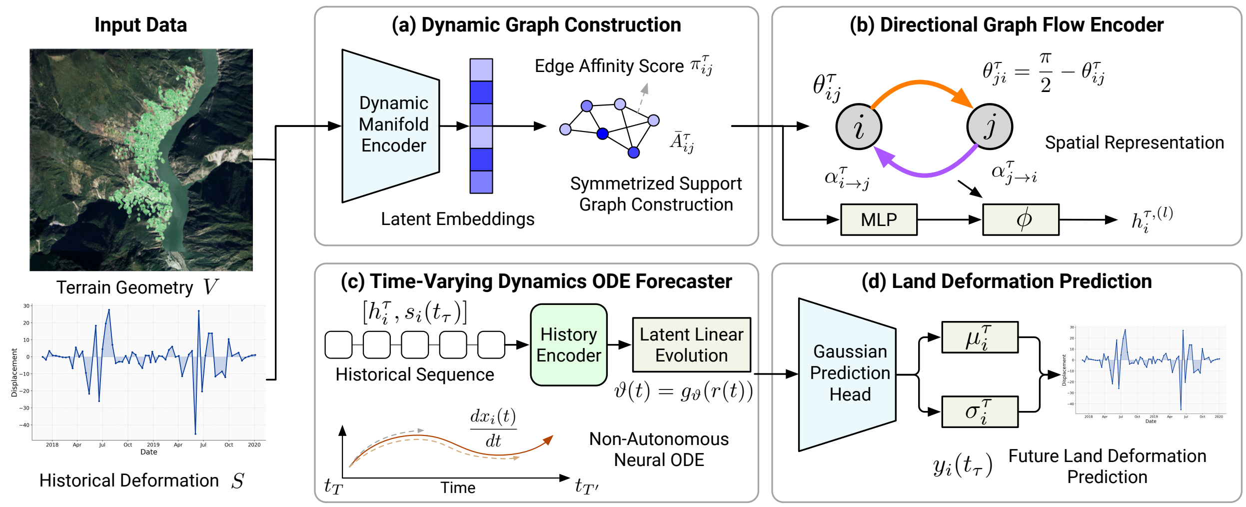

Fig. 1. Overview of the proposed DKLand framework. It consists of four stages: (1) deformation-aware dynamic graph construction, (2) directional graph-flow spatial encoding, (3) Koopman-inspired time-varying continuous dynamics, and (4) probabilistic land deformation prediction.

a) Continuous edge directionality: For each support edge (i,j) in $\bar{A}^{\tau}$, we assign a phase angle $\theta_{ij}^{\tau} \in [0, \pi/2]$, where small values indicate stronger influence from j to i, and large values indicate the opposite. To keep the two directions of the same edge pair coupled, we enforce

$$\theta_{ji}^{\tau} = \frac{\pi}{2} - \theta_{ij}^{\tau}. \tag{7}$$

The phase angle is predicted from pairwise geometry and deformation context:

$$\theta_{ij}^{\tau} = \frac{\pi}{2} \cdot \sigma\big(\mathrm{MLP}_{\theta}\big([\,v_i - v_j,\ s_i(t_\tau) - s_j(t_\tau)\,]\big)\big). \tag{8}$$

We then define the two directional flow weights as

$$\alpha_{j\to i}^{\tau} = \cos(\theta_{ij}^{\tau}), \qquad \alpha_{i\to j}^{\tau} = \sin(\theta_{ij}^{\tau}). \tag{9}$$

Because of Eq. (7), the two directions are complementary.

b) Directional message passing: Let $h_i^{\tau,(0)}$ denote the input feature of node i at time t_τ, initialized from terrain geometry and current deformation:

$$h_i^{\tau,(0)} = \mathrm{MLP}_{\mathrm{in}}([\,v_i;\ s_i(t_\tau)\,]). \tag{10}$$

At layer l, DKLand computes two directional aggregations:

$$m_{i,\mathrm{in}}^{\tau,(l)} = \sum_{j=1}^{N} \tilde{a}_{ij}^{\tau}\, \alpha_{j\to i}^{\tau}\, h_j^{\tau,(l-1)}, \tag{11}$$

$$m_{i,\mathrm{out}}^{\tau,(l)} = \sum_{j=1}^{N} \tilde{a}_{ij}^{\tau}\, \alpha_{i\to j}^{\tau}\, h_j^{\tau,(l-1)}. \tag{12}$$

The updated node representation is

$$h_i^{\tau,(l)} = \phi\Big(W_{\mathrm{self}}^{(l)} h_i^{\tau,(l-1)} + W_{\mathrm{in}}^{(l)} m_{i,\mathrm{in}}^{\tau,(l)} + W_{\mathrm{out}}^{(l)} m_{i,\mathrm{out}}^{\tau,(l)} + b^{(l)}\Big), \tag{13}$$

where $W_{\mathrm{self}}^{(l)}$, $W_{\mathrm{in}}^{(l)}$, and $W_{\mathrm{out}}^{(l)}$ are learnable parameters and $\phi(\cdot)$ is a nonlinearity. After L layers, we obtain

$$H^{\tau} = [h_1^{\tau,(L)}, \ldots, h_N^{\tau,(L)}] \in \mathbb{R}^{N \times d_h}.$$

The sequence $\{H^{\tau}\}_{\tau=1}^{T}$ is then passed to the continuous-time forecasting module.

E. Koopman-Inspired Time-Varying Dynamics ODE

Given the spatial representation sequence $\{H^{\tau}\}_{\tau=1}^{T}$, DKLand models future deformation evolution in continuous time. A standard neural ODE uses a fixed parameter set in the vector field, which can be restrictive under non-stationary deformation regimes [16], [18]. To improve adaptability, we introduce a Koopman-inspired non-autonomous ODE in which the dynamics parameters vary over time through a compact latent dynamics generator [19], [20].

a) Historical context and initial latent state: For each node i, we summarize the observed spatiotemporal history by

$$c_i = \mathrm{Enc}_{\mathrm{hist}}\Big(\big[[h_i^{\tau};\ s_i(t_\tau)]\big]_{\tau=1}^{T}\Big) \in \mathbb{R}^{d_c}, \tag{14}$$

where $\mathrm{Enc}_{\mathrm{hist}}(\cdot)$ is a temporal encoder. The initial latent state for forecasting is then

$$x_i(t_T) = \psi_{\mathrm{init}}(c_i) \in \mathbb{R}^{d_x}. \tag{15}$$

b) Latent linear evolution for time-varying dynamics: We introduce a global latent code $r(t) \in \mathbb{R}^{d_r}$ to control the time variation of the forecasting dynamics:

$$\frac{dr(t)}{dt} = Kr(t), \qquad r(t_T) = r_T, \tag{16}$$

where $K \in \mathbb{R}^{d_r \times d_r}$ is a learnable latent linear evolution matrix. Its initial condition is inferred from the observed spatiotemporal history:

$$r_T = \psi_r\Big(\big[\mathrm{Pool}([H^{\tau};\ S^{\tau}])\big]_{\tau=1}^{T}\Big). \tag{17}$$

The time-varying parameters of the neural vector field are then generated by

$$\vartheta(t) = g_{\vartheta}(r(t)), \tag{18}$$

where $g_{\vartheta}(\cdot)$ is a lightweight decoder.

c) Non-autonomous latent evolution: Conditioned on the global time-varying dynamics $\vartheta(t)$ and the node-specific history summary c_i, each node evolves according to

$$\frac{dx_i(t)}{dt} = f\big(x_i(t), t; \vartheta(t), c_i\big), \qquad t \in [t_T, t_{T'}]. \tag{19}$$

Here, $f(\cdot)$ is a neural vector field shared across nodes. Although Eq. (19) is node-wise, spatial dependence is preserved through the directional encoder outputs H^{τ} and through the shared global latent code $r(t)$.

We solve Eq. (16) and Eq. (19) using an adaptive ODE solver [16]. For each future timestamp $t_\tau \in \{t_{T+1}, \dots, t_{T'}\}$, the solver returns latent states $\{x_i(t_\tau)\}_{i=1}^{N}$.

F. Probabilistic Land Deformation Prediction

Given the future latent states, DKLand predicts both point estimates and uncertainty. We adopt a conditionally factorized likelihood:

$$p(Y \mid V, S) = \prod_{\tau=T+1}^{T'} \prod_{i=1}^{N} p(y_i(t_\tau) \mid x_i(t_\tau), c_i)\,. \tag{20}$$

Although the likelihood factorizes across nodes and forecast steps, the predictions remain coupled through the shared dynamic graph encoder and the continuous-time latent dynamics.

a) Gaussian prediction head: For each node i and forecast timestamp t_τ, we model

$$y_i(t_\tau) \mid x_i(t_\tau), c_i \sim \mathcal{N}\big(\mu_i^{\tau}, (\sigma_i^{\tau})^2\big), \tag{21}$$

where the mean and standard deviation are generated by a shared prediction head:

$$z_i^{\tau} = [x_i(t_\tau);\, c_i], \tag{22}$$

$$\mu_i^{\tau} = g_\mu(z_i^{\tau}), \tag{23}$$

$$\sigma_i^{\tau} = \mathrm{softplus}(g_\sigma(z_i^{\tau})) + \varepsilon. \tag{24}$$

Here, $g_\mu(\cdot)$ and $g_\sigma(\cdot)$ are shared MLPs and $\varepsilon > 0$ is a small constant.

b) Training objective: DKLand is trained by minimizing the Gaussian negative log-likelihood:

$$\mathcal{L}_{\mathrm{NLL}} = -\sum_{\tau=T+1}^{T'} \sum_{i=1}^{N} \log p(y_i(t_\tau) \mid x_i(t_\tau), c_i)\,, \tag{25}$$

which is equivalent to

$$\mathcal{L}_{\mathrm{NLL}} = \frac{1}{2} \sum_{\tau=T+1}^{T'} \sum_{i=1}^{N} \left[\log\big(2\pi(\sigma_i^{\tau})^2\big) + \frac{(y_i(t_\tau) - \mu_i^{\tau})^2}{(\sigma_i^{\tau})^2}\right]. \tag{26}$$

At inference time, μ_i^{τ} is used as the point forecast and σ_i^{τ} quantifies predictive uncertainty.

III. Experiments

We evaluate DKLand on real-world InSAR land deformation forecasting benchmarks. We first describe the datasets, baselines, evaluation metrics, and implementation details. We then present the main forecasting results, followed by an ablation study and a qualitative case study.

A. Experimental Settings

a) Data: We evaluate DKLand on two real-world landslide-prone InSAR datasets collected from the southwest of Sichuan province, China: HZY and PBG. The HZY dataset covers approximately nine months of observations (Nov. 30, 2018 to Sept. 8, 2019), while the PBG dataset covers about two years (Nov. 17, 2017 to Jan. 4, 2020). Each dataset is represented as an InSAR point cloud with 3D spatial coordinates and associated deformation time series. Following the standard protocol in DyLand, the data are split into training, validation, and test sets with ratios of 50%/30%/20%.

b) Baselines: We compare DKLand with a diverse set of representative baselines: (i) *heuristic and statistical methods*: HA(1), HA(3), SVR, and ARIMA [21]; (ii) *temporal deep learning methods*: GRU, LSTM, Bi-LSTM [11], Transformer, and NODE [16]; and (iii) *graph and spatiotemporal graph models*: GCN [22], STGCN [23], VGAE [24], SIG-VAE [25], P-GNN [26], STGODE [27], SA-GNN [28], and DyLand [15]. These baselines cover non-neural forecasting, sequence-only deep models, graph representation models, and recent spatiotemporal graph learning methods, providing a comprehensive comparison across different modeling paradigms.

c) Metrics and Implementation: Following DyLand, we evaluate forecasting performance using five metrics: root mean squared error (RMSE), mean absolute error (MAE), Accuracy (ACC), coefficient of determination (R^2), and explained variance score (EVS) [15]. For ACC, a prediction is counted as correct if its absolute error is no greater than 0.01, following the same definition as DyLand. Unless otherwise stated, we follow the preprocessing and optimization protocol of DyLand for fair comparison. The models are optimized with Adam using learning rate 10^{-3} and weight decay 10^{-5}; and early stopping is applied with a patience of 100 epochs. For continuous-time integration, we use the `dopri5` solver.

B. Main Results

Table I reports the main forecasting results on the four evaluation datasets. Overall, DKLand achieves the best performance on all 20 metric-subset combinations, demonstrating consistent advantages over both classical baselines and recent spatiotemporal neural models.

Compared with DyLand, DKLand yields consistent improvements on every subset. On HZY-West, DKLand reduces RMSE from 0.052 to 0.050 and MAE from 0.035 to 0.033. On HZY-East, the corresponding values improve from 0.060 to 0.058 and from 0.043 to 0.041. The gains are even more pronounced on the PBG datasets, where RMSE decreases from 0.013 to 0.011 on PBG-West and from 0.016 to 0.014 on PBG-East. DKLand also achieves the highest ACC, R^2, and EVS on all four datasets, indicating that the improvements are not limited to a single error criterion but remain consistent across multiple evaluation perspectives.

Several trends are clear from Table I. First, heuristic and statistical methods perform much worse than deep learning and graph-based models. This suggests that land deformation forecasting depends on complex nonlinear spatiotemporal patterns

TABLE I
MAIN LAND DEFORMATION PREDICTION RESULTS. LOWER IS BETTER FOR RMSE AND MAE. THE BEST AND SECOND-BEST RESULTS ARE HIGHLIGHTED IN BOLD AND UNDERLINE, RESPECTIVELY.

Dataset	**HZY-West**					**HZY-East**					**PBG-West**					**PBG-East**				
Metric	RMSE	MAE	ACC	R^2	EVS	RMSE	MAE	ACC	R^2	EVS	RMSE	MAE	ACC	R^2	EVS	RMSE	MAE	ACC	R^2	EVS
HA(1)	4.190	2.799	0.072	0.054	0.161	4.973	3.427	0.056	0.065	0.178	8.348	5.114	0.044	0.062	0.120	6.944	4.194	0.046	0.061	0.117
HA(3)	3.992	2.889	0.052	0.066	0.122	4.645	3.352	0.045	0.094	0.158	7.535	5.186	0.040	0.092	0.142	6.067	4.010	0.050	0.097	0.164
SVR	3.956	3.209	0.030	0.108	0.274	4.750	3.693	0.032	0.135	0.262	6.612	4.199	0.059	0.195	0.291	5.955	3.546	0.076	0.191	0.282
ARIMA	4.888	4.088	0.053	0.265	0.215	6.704	5.395	0.031	0.271	0.204	6.242	4.098	0.035	0.190	0.212	5.325	3.200	0.055	0.175	0.228
GRU	0.250	0.204	0.421	0.223	0.315	0.197	0.170	0.456	0.207	0.290	0.249	0.197	0.460	0.120	0.163	0.200	0.160	0.540	0.215	0.137
LSTM	0.241	0.200	0.433	0.230	0.317	0.192	0.168	0.460	0.213	0.295	0.248	0.195	0.461	0.122	0.164	0.195	0.156	0.548	0.220	0.139
Bi-LSTM	0.240	0.199	0.435	0.230	0.318	0.190	0.165	0.464	0.216	0.299	0.248	0.195	0.461	0.123	0.164	0.193	0.152	0.552	0.224	0.141
Transf.	0.130	0.099	0.614	0.389	0.425	0.143	0.107	0.480	0.387	0.366	0.074	0.045	0.551	0.277	0.258	0.080	0.045	0.696	0.337	0.349
NODE	0.076	0.057	0.527	0.407	0.458	0.101	0.075	0.506	0.469	0.417	0.052	0.044	0.584	0.283	0.291	0.053	0.041	0.710	0.401	0.412
GCN	0.100	0.076	0.442	0.365	0.332	0.103	0.078	0.440	0.399	0.343	0.063	0.050	0.574	0.204	0.208	0.089	0.056	0.662	0.385	0.345
VGAE	0.091	0.068	0.483	0.390	0.391	0.104	0.077	0.465	0.392	0.313	0.051	0.040	0.601	0.375	0.332	0.083	0.052	0.712	0.355	0.348
SIG-VAE	0.088	0.065	0.525	0.374	0.422	0.096	0.071	0.513	0.499	0.440	0.045	0.037	0.734	0.405	0.426	0.079	0.050	0.775	0.408	0.393
STGCN	0.069	0.055	0.533	0.456	0.451	0.078	0.057	0.562	0.563	0.573	0.040	0.029	0.815	0.447	0.488	0.041	0.027	0.854	0.437	0.426
P-GNN	0.065	0.048	0.628	0.423	0.466	0.071	0.051	0.637	0.507	0.516	0.031	0.020	0.908	0.474	0.491	0.032	0.026	0.911	0.441	0.449
STGODE	0.063	0.046	0.645	0.459	0.471	0.069	0.051	0.642	0.505	0.515	0.029	0.019	0.911	0.478	0.494	0.030	0.024	0.916	0.449	0.453
SA-GNN	0.058	0.037	0.718	0.488	0.483	0.062	0.048	0.698	0.497	0.501	0.021	0.015	0.964	0.492	0.480	0.024	0.018	0.956	0.470	0.478
DyLand	0.052	0.035	0.742	0.492	0.492	0.060	0.043	0.700	0.583	0.590	0.013	0.010	0.993	0.538	0.540	0.016	0.013	0.978	0.487	0.496
DKLand	**0.050**	**0.033**	**0.748**	**0.498**	**0.499**	**0.058**	**0.041**	**0.705**	**0.592**	**0.598**	**0.011**	**0.009**	**0.996**	**0.545**	**0.548**	**0.014**	**0.012**	**0.982**	**0.494**	**0.503**

TABLE II
ABLATION RESULTS ON THE HZY-WEST AND HZY-EAST DATASETS.

HZY-West	RMSE	MAE	ACC	R^2	EVS
DKLand w/o directional flow	0.054	0.036	0.739	0.488	0.490
DKLand w/o time dynamics	0.051	0.034	0.743	0.494	0.493
DKLand	0.050	0.033	0.748	0.498	0.499
HZY-East	RMSE	MAE	ACC	R^2	EVS
DKLand w/o directional flow	0.062	0.045	0.699	0.580	0.588
DKLand w/o time dynamics	0.060	0.044	0.701	0.583	0.591
DKLand	0.058	0.041	0.705	0.592	0.598

that simple methods cannot represent well. Second, sequence-only deep models such as GRU, LSTM, and Transformer perform much better than classical baselines, but they remain behind graph-based spatiotemporal models. This gap shows the value of modeling spatial relationships among monitored locations explicitly. Third, DyLand already provides a strong deformation-aware forecasting backbone. The additional gains of DKLand indicate that directional spatial propagation and time-varying continuous dynamics each improve the model beyond that baseline. Taken together, these results support the main claim of this paper. Better spatial interaction modeling and more adaptive temporal dynamics lead to more accurate land deformation forecasting across different terrain settings and deformation patterns.

C. Ablation Study

We conduct ablation studies to examine the contribution of the two key components introduced in DKLand: (1) the directional graph-flow encoder for anisotropic spatial modeling, and (2) the time-varying dynamics ODE forecaster for non-stationary continuous-time evolution. Table II reports the results on HZY-West and HZY-East datasets.

Removing either component degrades performance across all five metrics on both datasets, which shows that both contribute to the final model. On HZY-West, removing the directional graph-flow encoder increases RMSE from 0.050 to 0.054 and MAE from 0.033 to 0.036, while ACC, R^2, and EVS also decrease. On HZY-East, the same ablation increases RMSE from 0.058 to 0.062 and MAE from 0.041 to 0.045, again with consistent declines in the remaining metrics. These results indicate that explicitly modeling directional and asymmetric spatial interactions helps capture anisotropic terrain dependencies and improves spatial representations.

Removing the time-varying dynamics module also reduces performance on both datasets. On HZY-West, RMSE increases from 0.050 to 0.051 and MAE from 0.033 to 0.034. On HZY-East, RMSE increases from 0.058 to 0.060 and MAE from 0.041 to 0.044. ACC, R^2, and EVS also decrease in both cases. Although the performance drop is smaller than that caused by removing directional flow, the full DKLand model remains the best on all metrics for both datasets. This suggests that the time-varying dynamics module provides additional gains by better modeling non-stationary temporal evolution after spatial features have been extracted.

Overall, the ablation results show that the two proposed components are complementary. The directional graph-flow encoder contributes the larger gain on both datasets, while the time-varying dynamics module provides further improvement. Their combination gives the best overall performance.

D. Case Study

To provide a qualitative view of DKLand's prediction behavior, Fig. 2 presents a representative test case on the 3D terrain surface. The left panel shows the ground-truth deformation pattern, while the right panel visualizes the absolute prediction error at the corresponding spatial locations.

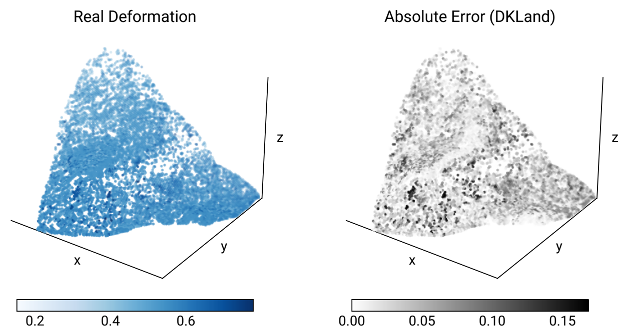

Fig. 2. Case study of DKLand on a representative test sample. Left: ground-truth deformation on the 3D terrain surface. Right: absolute prediction error of DKLand at the corresponding spatial locations.

DKLand captures the overall deformation structure well, and the prediction error remains small over most monitored points. A few localized areas show larger residuals, but these regions are sparse rather than widespread across the surface. This observation is consistent with the quantitative results in Table I. It suggests that DKLand captures the dominant terrain-related deformation pattern while maintaining stable prediction quality across most spatial locations.

IV. Conclusion

In this paper, we presented DKLand, a probabilistic spatiotemporal forecasting framework for land deformation prediction. DKLand builds on a deformation-aware dynamic graph backbone, strengthens spatial modeling through a directional graph-flow encoder, and improves temporal forecasting through a Koopman-inspired time-varying neural ODE. Experiments on two real-world InSAR datasets, HZY and PBG, show that DKLand consistently outperforms strong baselines, including DyLand. The ablation results also confirm that both proposed components contribute to the final performance. These findings show that combining directional spatial propagation with time-varying continuous dynamics is an effective approach for probabilistic land deformation forecasting.

References

[1] M. Liu, Z. Yang, W. Xi, J. Guo, and H. Yang, "InSAR-based method for deformation monitoring of landslide source area in Baihetan reservoir, China," *Frontiers in Earth Science*, vol. 11, p. 1253272, 2023.

[2] Q. Wang, Y. Gao, T. Gong, T. Liu, Z. Sui, J. Fan, and Z. Wang, "Dam surface deformation monitoring and analysis based on PS-InSAR technology: A case study of Xiaolangdi reservoir dam in China," *Water*, vol. 15, no. 18, p. 3298, 2023.

[3] M. H. Z. Putra, A. G. Suhadha, W. Hermawan, D. Sarah, R. Handika, E. Soebowo, and N. A. Satriyo, "Assessing regional surface subsidence and its impact on critical infrastructure in Gedebage, Bandung using SBAS InSAR analysis," in *IEEE International Conference on Aerospace Electronics and Remote Sensing Technology (ICARES)*, 2024, pp. 1–6.

[4] P. Zhang, Z. Guo, S. Guo, and J. Xia, "Land subsidence monitoring method in regions of variable radar reflection characteristics by integrating PS-InSAR and SBAS-InSAR techniques," *Remote Sensing*, vol. 14, no. 14, p. 3265, 2022.

[5] A. Ferretti, C. Prati, and F. Rocca, "Permanent scatterers in SAR interferometry," *IEEE Transactions on Geoscience and Remote Sensing (TGRS)*, vol. 39, no. 1, pp. 8–20, 2001.

[6] P. Berardino, G. Fornaro, R. Lanari, and E. Sansosti, "A new algorithm for surface deformation monitoring based on small baseline differential SAR interferograms," *IEEE Transactions on Geoscience and Remote Sensing (TGRS)*, vol. 40, no. 11, pp. 2375–2383, 2003.

[7] L. Ayalew and H. Yamagishi, "The application of GIS-based logistic regression for landslide susceptibility mapping in the Kakuda-Yahiko mountains, Central Japan," *Geomorphology*, vol. 65, pp. 15–31, 2005.

[8] A. Merghadi, A. P. Yunus, J. Dou, J. Whiteley, B. ThaiPham, D. T. Bui, R. Avtar, and B. Abderrahmane, "Machine learning methods for landslide susceptibility studies: A comparative overview of algorithm performance," *Earth-Science Reviews*, vol. 207, p. 103225, 2020.

[9] P. Reichenbach, M. Rossi, B. D. Malamud, M. Mihir, and F. Guzzetti, "A review of statistically-based landslide susceptibility models," *Earth-Science Reviews*, vol. 180, pp. 60–91, 2018.

[10] Y. Li, B. Fu, Y. Yin, X. Hu, W. Wang, W. Wang, X. Li, and G. Long, "Review on the artificial intelligence-based methods in landslide detection and susceptibility assessment: Current progress and future directions," *Intelligent Geoengineering*, vol. 1, no. 1, pp. 1–18, 2024.

[11] Z. Lin, X. Sun, and Y. Ji, "Landslide displacement prediction based on time series analysis and double-BiLSTM model," *International Journal of Environmental Research and Public Health*, vol. 19, no. 4, 2022.

[12] Y. Sun, T. Liu, C. Zhang, N. Xi, and H. Wang, "Spatiotemporal prediction of landslide displacement using graph convolutional network-based models: A case study of the Tangjiao 1# landslide in Chongqing, China," *Applied Sciences*, vol. 14, no. 20, p. 9288, 2024.

[13] M. A. Khalili, L. Guerriero, M. Pouralizadeh, D. Calcaterra, and D. Di Martire, "Monitoring and prediction of landslide-related deformation based on the GCN-LSTM algorithm and SAR imagery," *Natural Hazards*, vol. 119, no. 1, pp. 39–68, 2023.

[14] B. Hu, W. Li, W. Lu, F. Zhao, Y. Li, and R. Li, "Integrating InSAR data and LE-Transformer for foundation pit deformation prediction," *Remote Sensing*, vol. 17, no. 6, p. 1106, 2025.

[15] X. Xu, T. Zhong, F. Zhou, R. Li, G. Trajcevski, and Q. Meng, "Learning spatiotemporal manifold representation for probabilistic land deformation prediction," *IEEE Transactions on Cybernetics*, vol. 54, no. 1, pp. 572–585, 2024.

[16] R. T. Chen, Y. Rubanova, J. Bettencourt, and D. K. Duvenaud, "Neural ordinary differential equations," in *NeurIPS*, 2018, pp. 1–13.

[17] S. H. Pahng and S. Hormoz, "Improving graph neural networks by learning continuous edge directions," in *International Conference on Learning Representations (ICLR)*, 2025, pp. 1–15.

[18] H. Bai and W. Ding, "KoNODE: Koopman-driven neural ordinary differential equations with evolving parameters for time series analysis," in *International Conference on Machine Learning*, 2025, pp. 1–11.

[19] B. O. Koopman, "Hamiltonian systems and transformation in hilbert space," *Proceedings of the National Academy of Sciences*, vol. 17, no. 5, pp. 315–318, 1931.

[20] I. Mezić, "Spectral properties of dynamical systems, model reduction and decompositions," *Nonlinear Dynamics*, vol. 41, no. 1, pp. 309–325, 2005.

[21] Y. Wang, H. Tang, J. Huang, T. Wen, J. Ma, and J. Zhang, "A comparative study of different machine learning methods for reservoir landslide displacement prediction," *Engineering Geology*, vol. 298, p. 106544, 2022.

[22] T. N. Kipf and M. Welling, "Semi-supervised classification with graph convolutional networks," in *International Conference on Learning Representations (ICLR)*, 2017, pp. 1–14.

[23] B. Yu, H. Yin, and Z. Zhu, "Spatio-temporal graph convolutional networks: A deep learning framework for traffic forecasting," in *International Joint Conference on Artificial Intelligence (IJCAI)*, 2018, pp. 3634–3640.

[24] T. N. Kipf and M. Welling, "Variational graph auto-encoders," *arXiv:1611.07308*, pp. 1–3, 2016.

[25] A. Hasanzadeh, E. Hajiramezanali, K. Narayanan, N. Duffield, M. Zhou, and X. Qian, "Semi-implicit graph variational auto-encoders," *NeurIPS*, pp. 1–12, 2019.

[26] W. Shi and R. Rajkumar, "Point-GNN: Graph neural network for 3D object detection in a point cloud," in *CVPR*, 2020, pp. 1711–1719.

[27] Z. Fang, Q. Long, G. Song, and K. Xie, "Spatial-temporal graph ODE networks for traffic flow forecasting," in *ACM SIGKDD Conference on Knowledge Discovery and Data Mining (KDD)*, 2021, pp. 364–373.

[28] F. Zhou, R. Li, G. Trajcevski, and K. Zhang, "Land deformation prediction via slope-aware graph neural networks," in *AAAI Conference on Artificial Intelligence*, vol. 35, no. 17, 2021, pp. 15 033–15 040.